Effects of oxide morphology on lithium-ion conductivity of $LiBH_4$-Al_2O_3 composites

Hiroki Mizuochi[1], Yuki Nakagawa[2]*, Tamaki Shibayama[2], Yuchen Yao[3], Fangqin Guo[3], Hiroki Miyaoka[4], Takayuki Ichikawa[3]

[1] Graduate School of Engineering, Hokkaido University, N-13 W-8, Sapporo, 060-8628, Japan
[2] Faculty of Engineering, Hokkaido University, N-13 W-8, Sapporo, 060-8628, Japan
[3] Graduate School of Advanced Science and Engineering, Hiroshima University, 1-4-1 Kagamiyama, Higashi-Hiroshima, 739-8527, Japan
[4] Natural Science Center for Basic Research and Development, Hiroshima University, 1-3-1 Kagamiyama, Higashi-Hiroshima, 739-8530, Japan

* Corresponding author
*E-mail: y-nakagawa@eng.hokudai.ac.jp (Y. Nakagawa)

Keywords
Solid Electrolytes, Lithium-Ion Batteries, Dynamics, Solid-State NMR, Complex Metal Hydrides

Abstract
The ionic conductivity of $LiBH_4$-Al_2O_3 composites was investigated, focusing on the effect of oxide morphology and surface functional groups. Composites were prepared by mixing mesoporous Al_2O_3 (wormhole), gamma Al_2O_3, and nanofiber Al_2O_3. All composites showed an improvement in ionic conductivity, with the 55 wt% mesoporous composites showing the highest ionic conductivity (4.6×10^{-5} S cm^{-1} at 30 °C) and lowest activation energy for ionic conduction (0.53 eV for 30–100 °C). Notably, ^7Li static nuclear magnetic resonance revealed that only the mesoporous composites exhibited a motionally narrowed line, indicative of highly mobile lithium ions. The proportion of highly mobile lithium ions in all composites was found to correlate with the specific surface area and specific pore volume of each Al_2O_3 type. Multiple structural analyses indicated the existence of fast lithium-ion conduction layers at the interface between $LiBH_4$ and Al_2O_3. Additionally, the influence of mesoporous Al_2O_3 surface functional groups on ionic conductivity was explored. This study highlights the potential of using different oxide morphologies to better understand and visualize ionic conductivity enhancement interfaces.

1. Introduction

The pursuit of efficient energy storage devices is critical for achieving a sustainable society. Electrochemical energy storage in rechargeable batteries is particularly attractive and finds widespread use in applications ranging from wearable devices to electric vehicles. All-solid-state batteries are expected to exceed conventional liquid lithium-ion batteries in some key performance areas, notably enhancing safety. By replacing the flammable organic solvents in the electrolyte with a solid electrolyte, these batteries eliminate ignition risks and prevent electrolyte leakage.[1–3] Furthermore, their compatibility with lithium metal and other high-energy-density materials broadens the range of electrode materials, leading to performance levels that can exceed those of conventional liquid lithium-ion batteries.[4] For these reasons, all-solid-state batteries have garnered significant attention in recent years. However, designing suitable solid electrolytes that combine sufficient chemical and electrochemical stability with high ionic conductivity remains a major challenge. A variety of electrolytes have been identified to date. Among these, complex metal hydrides, such as $LiBH_4$, $Li_2B_{12}H_{12}$, $LiAlH_4$, Li_3AlH_6, $LiNH_2$, Li_2NH, $Li(NH_3)_nBH_4$, stand out.[5–11] $LiBH_4$, in particular, shows promising candidates for a solid electrolyte. Compared to oxide, sulfide, and polymer-based ionic conductors,[12–14] complex metal hydrides exhibit several advantageous properties as solid electrolytes for all-solid-state batteries. For instance, $LiBH_4$ is characterized by a low density due to its composition of light elements. It also offers high flexibility and excellent electrochemical stability against Li metal electrodes. In other words, it is possible to achieve a material that combines low weight, high electrochemical stability (up to 3 V vs. Li/Li^+), and the ability to form a good interface with Li electrode materials. These unique features distinguish it from most other solid ionic conductors. A notable characteristic of $LiBH_4$ is its structural phase transition from the orthorhombic low-temperature (LT) phase to the hexagonal high-temperature (HT) phase at around 110 °C.[5] The HT phase exhibits high ionic conductivity of $\sim 10^{-3}$ S cm^{-1}. However, the ionic conductivity of $LiBH_4$ in the LT phase drops significantly to $\sim 10^{-8}$ S cm^{-1} at 30 °C.[15] Therefore, ongoing research focuses on enhancing the ionic conductivity of $LiBH_4$ at ambient temperature.

It has been reported that the ionic conductivity of $LiBH_4$ at ambient temperature can be improved through high-energy ball milling. This enhancement is caused by defects and a disordered lattice structure created during the high-energy ball milling process.[11,16] The conduction in $LiBH_4$ is thought to occur via lattice defects through an interstitial mechanism.[17] However, the ionic conductivity gradually decreases with each cycle, indicating instability during repeated cycling.[18] Solid solutions of lithium halide, such as LiI, LiBr, and LiCl in $LiBH_4$, can also improve ionic conductivity at ambient temperature. X-ray diffraction shows that the HT phase is detected even at ambient temperatures below the structural phase transition temperature. This is attributed to the stabilization of the conductive HT phase at ambient temperature. By replacing some of the BH_4^- anions with other anions, a homogeneous solid solution is formed, improving ionic conductivity.[19–23]

A different approach to enhance ionic conductivity involves nanocomposite formation by mixing $LiBH_4$ with metal oxides.[24–27] Ionic conductivity improvements have been observed in nanocomposite synthesized through both high-energy ball milling and melt-infiltration techniques. Reports indicate that nanocomposites formed with high-surface-area or nanoporous oxides exhibit ionic conductivities up to three orders of magnitude higher than that of pristine $LiBH_4$ at ambient temperature.[28,29] This enhancement has been observed in various metal oxides, e.g., ZrO_2, MgO, TiO_2, Al_2O_3, SiO_2, and CaO.[18] While the exact mechanism behind the enhancement in ionic conductivity through nanocomposite formation is not fully understood, it is known that conductor-insulator interface effects are important. These effects may arise from the formation of a space charge layer, the development of a tertiary phase, or the stabilization of a conductive polymorph in the lithium-ion conductor.[30–35]

In this study, we focus on the interface between $LiBH_4$ and Al_2O_3 in composite lithium-ion conductors to investigate the mechanism of ionic conductivity enhancement. Although the effects of silica surface groups on the conductivity of $LiBH_4$-SiO_2 composites were investigated,[36] the effects of Al_2O_3 surface properties have not been clarified yet. Thus, we selected Al_2O_3 with distinct particle structures, i.e., mesoporous Al_2O_3 (wormhole), gamma Al_2O_3, and nanofiber Al_2O_3, as the metal oxide to be added to $LiBH_4$. The effects of these particle morphologies on ionic conductivity are discussed. Although the mesoporous SiO_2 with one-dimensional channels of mesopores (MCM-41 or SBA-15) was used as the host oxides in the previous studies,[25–27] the three-dimensional wormhole mesoporous Al_2O_3 was selected in this study for improving the conductivity. Gamma Al_2O_3 is also a kind of porous material with three-dimensional nanostructures. Different from these oxides, one-dimensional fiber Al_2O_3 with low porosity was selected to confirm the porosity and dimensionality effects of oxides.

2. Experimental Section

2.1. Sample synthesis

All samples were handled in an argon-filled glovebox with an O_2 concentration below 2 ppm. $LiBH_4$ (purity 95%, Strem), mesoporous Al_2O_3 (purity N.A., Sigma Aldrich), gamma Al_2O_3 (purity 99.99%, Kojundo Chemical Lab. Co., Ltd.), and nanofiber Al_2O_3 (purity ≥ 90%, Sigma Aldrich) powders were used as received. Mechanical ball milling was performed using a planetary ball-milling apparatus (Fritsch, Pulverisette 7, Cr steel vessel with 15 zirconia balls). The ball-to-powder weight ratio was 75:1. In this study, composite materials with different coating thicknesses of $LiBH_4$ on Al_2O_3 were prepared, primarily with 55 wt% and 83 wt% Al_2O_3. The two different weight fractions of Al_2O_3 (55 and 83 wt% corresponding to 17 and 45 vol% of Al_2O_3, respectively) were ball milled at 400 rpm for 0.5 h in an Ar atmosphere to produce uniform composites. To study the effect of surface functional groups on ionic conductivity, surface conditions were modified via a vacuum heat treatment for 6 h at various temperatures.

2.2. Characterization

The surface structure of each Al_2O_3 particle was observed with a field emission gun scanning electron microscopy (FEGSEM, JEOL, JSM-7001FA, accelerating voltage of 15 kV) and transmission electron microscopy (TEM, JEOL, 2000FX, accelerating voltage of 200 kV). The average pore diameter, specific pore volume, and specific surface area of each Al_2O_3 particle were determined using the Brunauer-Emmett-Teller (BET, Yuasa Ionics, Autosorb 6AG AP-100021) model for N_2-physisorption isotherms. The composite state of $LiBH_4$ and Al_2O_3 was observed using high-angle annular dark-field scanning TEM (HAADF-STEM) and energy-dispersive X-ray spectroscopy (STEM-EDS) using a spherical aberration-corrected STEM (Cs-corrected STEM, FEI, Titan^3 G2 60-300, accelerating voltage of 300 kV). Powder samples were dispersed on a Quantifoil copper grid and transported under an inert atmosphere using an Atmos Defend Holder (Mel-Build).

The crystalline phase of samples was analyzed using X-ray diffraction (XRD, Rigaku SmartLab, with Cu Kα radiation). The XRD samples were covered with a polyimide sheet in a glovebox to prevent contact with air. For ionic conductivity measurements, sample powders were pressed into a pellet (7 mm diameter, ~2 mm thick). The ionic conductivities were measured using an alternating current impedance analyzer (AC impedance, HIOKI, IM3536) at temperatures ranging from 30 to 140°C in 10°C increments at a frequency range between 4 Hz and 8 MHz. Lithium foils (purity 99.9%, Alfa Aesar, thickness of 0.75 mm) were used as electrodes. Electronic conductivities were analyzed using a direct current polarization analyzer (DC impedance, Bio-Logic SAS: SP-150). Chemical bonding states and lithium-ion dynamics were investigated using solid-state nuclear magnetic resonance (solid-state NMR, Bruker, Avance Neo 500) under a magnetic field of 11.74 T. The 3.2 mm Bruker ZrO_2 rotors were filled with the powder samples. The ^{1}H, ^{6}Li, ^{11}B, and ^{27}Al magic-angle spinning (MAS) spectra were acquired with pulse widths of 4.0, 1.6, 2.0, and 1.7 μs, respectively. The corresponding recycle delays were 10, 30, 5, and 2 s, respectively. Additionally, ^{7}Li static NMR spectra were acquired using a single-pulse experiment with a pulse width of 3.8 μs. The MAS NMR spectra were recorded at a spinning speed of 20 kHz.

3. Results and Discussion

3.1. Nanostructure analysis of Al_2O_3 and the $LiBH_4$-Al_2O_3 composites

Three types of Al_2O_3 with different particle microstructures were used in this study: mesoporous Al_2O_3 (wormhole), gamma Al_2O_3, and nanofiber Al_2O_3. The mesoporous Al_2O_3 utilized here is of the ''wormhole'' type, named for its random and scattered pore orientations, unlike the ordered mesoporous SiO_2 or Al_2O_3 often used in previous studies.[25,26,35] Table 1 shows the average pore diameter, specific pore volume, and specific surface area of each Al_2O_3 particle based on BET analysis. SEM and TEM images of the Al_2O_3 samples are shown in Figure 1 and Figure 2, respectively. The particle sizes of three types of Al_2O_3 were examined using SEM and TEM analysis. The particle sizes of mesoporous Al_2O_3 and gamma Al_2O_3 were found to be 5–30 μm and 0.3–2 μm, respectively. For nanofiber Al_2O_3, the fiber diameter ranged from 0.2–1 μm,

and the fiber length ranged from 0.3–30 μm. Mesoporous Al_2O_3 had a relatively large particle size; however, it had a porous structure and the largest specific surface area among the three Al_2O_3 samples. Gamma Al_2O_3 had a smaller particle size and specific surface area compared with mesoporous Al_2O_3. The difference in specific pore volume between mesoporous and gamma Al_2O_3 was not as pronounced as the difference in specific surface area. TEM images show that nanofiber Al_2O_3 had a fiber-like structure and exhibited the lowest specific pore volume and specific surface area of the three.

STEM analysis was performed on the 55 wt% mesoporous Al_2O_3 composite. The $LiBH_4$-ZrO_2 system has been analyzed in a previous study.[28] Figure S1 presents TEM images of the 55 wt% mesoporous composite, while Figure 3 shows the HAADF-STEM image (a) and the corresponding STEM-EDS maps for B (b), Al (c), B overlayed with Al (d) and O (e). The distribution of B covered a broader area than that of Al, indicating that $LiBH_4$ effectively coated the mesoporous Al_2O_3. Conversely, the O distribution closely matched that of B and was wider compared with Al. This observation can be explained by two possible mechanisms: (1) $LiBH_4$, being a reductant, may have undergone a redox reaction with Al_2O_3 during the ball milling process, or (2) the mesoporous Al_2O_3, rich in physisorbed water and hydroxy groups, reacted with $LiBH_4$. Indeed, the formation of B-O species (i.e., $LiBO_2$ or $LiB(OH)_4$) was observed in the ^{11}B MAS NMR spectra, as shown in Section 3.3.

3.2. Ionic conductivity and lithium-ion dynamics

This section discusses the effect of mixing each Al_2O_3 sample with $LiBH_4$ on ionic conductivity. AC impedance measurements were analyzed in 10 °C increments, from 30 to 140 °C. Figure 4 shows the ionic conductivity of pristine $LiBH_4$, 55 wt% mesoporous, 55 wt% gamma, and 55 wt% nanofiber. Additionally, Figure S2 shows the conductivity of pristine $LiBH_4$ and 83 wt% Al_2O_3. Table S1 provides the coating thickness, pore filling rate, activation energy (E_a), and ionic conductivity of all composites. The E_a values were calculated by using the Arrhenius equation: $\sigma = \sigma_0 \exp(-E_a/\mathrm{k}T)$, where σ is ionic conductivity, σ_0 is the pre-exponential factor, E_a is the activation energy, k is the Boltzmann constant, and T is the absolute temperature. The coating thickness was calculated using the specific surface area obtained from BET analysis, assuming uniform coverage of $LiBH_4$. The pore filling rate was also calculated using the specific pore volume obtained from BET analysis, under the assumption that all the $LiBH_4$ penetrated into Al_2O_3 pores. Regarding the possibility of pore filling via ball milling, it could be achievable to some extent, but not fully. Figure S3 shows the N_2 adsorption isotherms of the 83 wt% and 100 wt% mesoporous Al_2O_3 obtained by BET method. The isotherm of 100 wt% Al_2O_3 shows a capillary condensation step at a relative pressure of 0.4-0.8, the 83 wt% mesoporous Al_2O_3 shows a small step at a high relative pressure above 0.9. This result suggests that milling could lead to mesopore filling and form macropores in some regions. However, as shown in Table S1, the theoretically ideal pore filling rate for the 83 wt% mesoporous material is 65 %, indicating a

discrepancy exists. Since the current BET measurements data are insufficient for quantitative evaluation, this will be addressed in future research. Coating thickness of $LiBH_4$ in the composite from the BET analysis was roughly consistent with the observed thickness from TEM in $LiBH_4$-ZrO_2 system. As shown in our previous study, the $LiBH_4$ thickness for 75 wt% nano ZrO_2 composite was less than 30 nm from TEM observation,[28] and this was consistent with the estimated thickness of 17.9 nm from the BET analysis as shown in Table S2 and S3. The specific surface area of ZrO_2 were smaller than those of Al_2O_3, and pore diameter of ZrO_2 was larger than that of Al_2O_3. Thus, the validity of BET measurement estimation for coating thickness and pore filling rate of $LiBH_4$ would be increased for the systems with small specific surface area and large pore sizes.

Compared to pristine $LiBH_4$, all 55 wt% Al_2O_3 samples demonstrated approximately 1000-fold higher ionic conductivity at ambient temperatures. The 55 wt% mesoporous Al_2O_3 composite had the highest ionic conductivity of 4.6×10^{-5} S cm^{-1} at 30 °C, followed by 55 wt% gamma Al_2O_3 at 1.9×10^{-5} S cm^{-1}, and 55 wt% nanofiber Al_2O_3 at 7.4×10^{-6} S cm^{-1}. This variation in ionic conductivity is attributed to differences in the microstructure of the Al_2O_3, which correlates with its specific surface area and pore volume. AC impedance measurements were conducted on two samples of 55 wt% mesoporous materials synthesized under the same conditions in a ball milling. As shown in the Figure S4, the variation was minimal, and it is likely that sample-to-sample variation would be small for the 55 wt% mesoporous composite.

The E_a values are indicated in Figures 4 and S2. The change in E_a that occurred between 55 wt% Al_2O_3 and 83 wt% Al_2O_3 is discussed. For the $LiBH_4$-Al_2O_3 composites with gamma and nanofiber Al_2O_3, the E_a remained unchanged regardless of the Al_2O_3 mixing ratio. Contrastingly, the E_a of mesoporous Al_2O_3 decreased from 0.53 eV at 55 wt% to 0.44 eV at 83 wt%, a reduction of ~0.1 eV, likely because of nanoconfinement effects. Table S1 shows that among all the composites, the 83 wt% mesoporous Al_2O_3 had the lowest pore filling rate of 65%. This suggests that the E_a of 83 wt% mesoporous Al_2O_3 is low because lithium-ion diffusion is primarily confined to the $LiBH_4$-Al_2O_3 interface, which is strongly influenced by nanoconfinement. The reason for the lower ionic conductivity of 83 wt% mesoporous Al_2O_3 compared with 83 wt% gamma Al_2O_3 is likely because the mesoporous sample is further from the optimal percolation threshold for lithium-ion diffusion.

DC impedance was used to verify the electronic conductivity of the composites. Two symmetric cells were prepared for each composite, using Li/$LiBH_4$-Al_2O_3/Li and Mo/$LiBH_4$-Al_2O_3/Mo, with an applied voltage of +0.5 V in both setups. As shown in Figure 5, very low currents of 0.001–0.002 μA were detected in Mo/$LiBH_4$-Al_2O_3/Mo, while thousands of times larger currents of 5-20 μA in Li/$LiBH_4$-Al_2O_3/Li cells. This suggests negligible electronic conductivity in the composites when Mo was used as counter electrodes, indicating that $LiBH_4$-Al_2O_3 composites behave as almost pure lithium-ion conductors.

Figure 6 shows the results of the ^{7}Li static NMR measurements conducted at 24 and 50 °C. A

notable difference in peak shape was observed in the 55 wt% mesoporous sample compared to the other composites. All spectra were fitted with two Gaussian components, revealing a sharp peak, known as a motionally narrowed line, solely in the 55 wt% mesoporous sample. In contrast, the 55 wt% gamma and nanofiber samples mostly exhibited broad peaks that could not be clearly separated by fitting. The motionally narrowed line represents highly mobile lithium ions moving along the fast diffusion pathways in the interfacial regions.[37] In previous studies using $LiBH_4$-LiI/Al_2O_3, a difference in the appearance of the motionally narrowed line was observed between bulk-conducting $LiBH_4$-LiI and interface-conducting $LiBH_4$-Al_2O_3.[38] When comparing the two, the sharpened motionally narrowed line below 30 °C is primarily attributed to the interface effects of $LiBH_4$-Al_2O_3. Therefore, the sharpened peak observed in this study is significantly influenced by the interface conduction of $LiBH_4$-Al_2O_3. The fraction of motionally narrowed lines in the 55 wt% mesoporous, gamma, and nanofiber composites at 24 °C were 10.0%, 6.2%, and 5.7%, respectively. The 55 wt% mesoporous sample displayed nearly twice the fraction of mobile lithium ions compared to the other composites. Similarly, the specific surface area of mesoporous Al_2O_3 was several times higher than that of other Al_2O_3. The specific surface area correlates with the fraction of motionally narrowed lines, which likely results from the fast Li conduction layers at $LiBH_4$-Al_2O_3 interfaces. The high conductivity of mesoporous Al_2O_3 is a result of its surface area. We performed ^{7}Li static NMR on 83 wt% mesoporous samples, and the results are shown in Figure S5. Despite the room-temperature ionic conductivity of the 83 wt% mesoporous sample being nearly identical to that of the 55 wt% nanofiber sample, the NMR spectra of the 83 wt% mesoporous sample exhibits narrower peaks compared to those of the 55 wt% gamma and nanofiber samples. This suggests that in systems such as $LiBH_4$-Al_2O_3, where fast conductive layers are formed at the interface, narrowing peaks due to the interfacial conductive layer are more pronounced when the oxide has a larger specific surface area.[38] This phenomenon was captured in the NMR results of the present study. In addition, a recent study suggested that differences in the charging states of the oxide may also affect the interface interactions between $LiBH_4$ and Al_2O_3.[39] Further research should explore the impact of these charging states in greater detail.

To analyze the optimal mixing ratio of $LiBH_4$ and Al_2O_3 for achieving the best percolation, impedance measurements were also conducted on a 70 wt% mesoporous sample, which lies between the 55 wt% and 83 wt% compositions. The ionic conductivities of the X wt% mesoporous materials with X= 55, 70, and 83 wt% at 30 °C were plotted in Figure S6. The optimal additive amount for the highest ionic conductivity lies between 55 and 83 wt%.

3.3. Structural analysis

The XRD profiles of the composites and pristine $LiBH_4$ are shown in Figure 7. The measurements shown in Figures 7 (a) and 7 (b) were performed at room temperature and 140 °C, respectively. In all composites, the diffraction peaks corresponded only to $LiBH_4$ and γ-Al_2O_3. It

is known that the diffraction peaks only appear at low angles of ~5° or less for mesoporous Al_2O_3,[40,41] indicating that the peak of γ-Al_2O_3 did not appear in the 55 wt% mesoporous composite. Importantly, no shift in the peak positions of $LiBH_4$ was observed in any of the composites, suggesting that no solid solutions were formed. In all composites, the crystal structure of $LiBH_4$ changed from orthorhombic to hexagonal around the structural phase transition temperature. The peak intensity of $LiBH_4$ in the composites decreased and broadened slightly relative to pristine $LiBH_4$. While this could be partly attributed to the lower $LiBH_4$ content in the measured samples, mechanical milling also likely contributed by reducing crystallinity and introducing lattice strain and defects. Notably, the peak intensity of $LiBH_4$ was lowest for the 55 wt% mesoporous composites compared to the other samples at both room temperature and 140 °C, which may be because of the large specific surface area of mesoporous Al_2O_3. This suggests that the $LiBH_4$-Al_2O_3 interface is less crystalline and more amorphous-like in nature.

The ^1H MAS NMR spectra in Figure 8 provides further insight. In the pristine $LiBH_4$ spectrum, a slight peak at 4.1 ppm was observed alongside the main peak at –0.5 ppm that represents BH_4^- bonding. The 4.1 ppm peak was caused by H_2 gas.[42] Multiple signals at 1.9, 3.4, 3.8, and 4.7 ppm were observed in the mesoporous, gamma, and nanofiber Al_2O_3 samples. The broad peak at around 4.7 ppm, observed in mesoporous Al_2O_3, likely results from physisorbed water on the surface,[43] while the 3.8, 3.4, and 1.9 ppm peaks in mesoporous and gamma Al_2O_3 correspond to hydroxy groups. The different peak positions are influenced by the isolated terminal, along with the double- and triple-bridged hydroxy groups,[44] with the 3.8 and 3.4 ppm peaks attributed to triple-bridged hydroxy groups and the 1.9 ppm peak corresponding to double-bridged hydroxy groups.

The ^6Li MAS NMR spectra for pristine $LiBH_4$, 55 wt% mesoporous, 55 wt% gamma, and 55 wt% nanofiber composites are shown in Figure 9 (a). A peak at –1.3 ppm, corresponding to $LiBH_4$ bonding, was observed in all samples, although all the composite samples exhibited a slight downfield shift from this position. Moreover, the 55 wt% mesoporous composites displayed a distinct low-field-shifted shoulder on the peak at –0.8 ppm, which may represent lithium states at the $LiBH_4$-Al_2O_3 interface. The peak position at –0.8 ppm was not consistent with the peak position of the products that are produced by the mixing of $LiBH_4$ and Al_2O_3.[45,46] As the chemical shift represents the electron density around the measured nucleus, this low-field shift suggests some differences in lithium environments at the interface.

The ^{11}B and ^{27}Al MAS NMR spectra are shown in Figures 9 (b) and 9 (c). In the ^{11}B MAS NMR spectra, a prominent signal for BH_4^- at –41.3 ppm was observed in all composites with no significant shifts. A low-intensity peak was observed at around 1.3 ppm solely in the 55 wt% mesoporous composite, indicating B-O bonds. This could result from a reaction between the small amount of physisorbed water in mesoporous Al_2O_3 with $LiBH_4$, generating $LiBO_2$ or $LiB(OH)_4$.[47,48] These B-O bonds likely arise from an intermediate layer at the $LiBH_4$-Al_2O_3 interface, although they may not represent the local interface structure because of possible

exposure to air during the experiment.[34] A previous study suggests that boron oxide species were not an essential component for the formation of a dynamic $LiBH_4$ layer.[39] The ^{27}Al MAS NMR was measured for the 55 wt% mesoporous, 55 wt% gamma, and 55 wt% nanofiber composites. Each spectrum showed two main peaks at 9 and 68 ppm, corresponding to six-coordinate (VI) and four-coordinate (IV) Al, respectively.[44] Interestingly, the 55 wt% mesoporous composite had less four-coordinate Al relative to six-coordinate Al.

In $LiBH_4$-Al_2O_3, where lithium-ion conduction benefits from interfacial effects, a percolating conductor-insulator pathway is expected. To facilitate rapid ion transport over long distances, it is advantageous to use a metal oxide with a large surface area. The E_a derived from the Arrhenius equation was 0.53 eV for the 55 wt% mesoporous composite and 0.44 eV for the 83 wt% mesoporous composite, indicating that lithium ions exhibit greater mobility at the interface, where they are nanoconfined within the pores.[49] In the high-temperature phase above 120 °C, the ionic conductivity of the 55 wt% gamma and 55 wt% nanofiber composites was nearly the same as that of pristine $LiBH_4$. Contrastingly, the ionic conductivity of the 55 wt% mesoporous composite was approximately twice that of $LiBH_4$ (Figure 4). This enhancement is likely caused by the interfacial effect stemming from the large specific surface area of mesoporous Al_2O_3 and the nanoconfinement of $LiBH_4$ within its pores, resulting in improved ionic conductivity compared to hexagonal $LiBH_4$.

From the structural analyses, the formation of amorphous-like layer was suggested and different chemical bonding states were shown for the composites between $LiBH_4$ and Al_2O_3 with a large surface area. Among three hypotheses for the origins of the enhanced conductivity in $LiBH_4$-oxide composites shown in the introduction, the stabilization of HT phase seems to be unlikely. The space charge region and the formation of the ternary phase are possible reasons, but further research is required. However, it seems more likely that the formation of the ternary phase plays a significant role. A prior study utilized X-ray Raman spectroscopy (XRS), a promising method for investigating battery materials and interfaces with low atomic numbers.[34] In the case of boron-based hydrides ($LiBH_4$ and $NaBH_4$), the original tetragonal (BH_4) structure transforms into a trigonal boron structure, resembling the "B—O" bonding in —BH_3. Additionally, at the interface, some Li and Na atoms are bonded to oxygen, suggesting the presence of M—O bonds. Metal hydride-oxide interfaces are known to have a high density of defects, making it difficult to fully understand their complex structures. However, it has been shown that the formed interface is strongly influenced by the physical and chemical properties of the oxide used. In other words, surface reactions play a dominant role in the interfacial ion dynamics, and a direct correlation has been established between the nature of interfacial phases and ion mobility in nanocomposite solid electrolytes.

3.4. Surface properties of mesoporous Al_2O_3

To investigate the effect of physisorbed water and the density of hydroxy groups on the surface

of mesoporous Al_2O_3 on ionic conductivity, we performed vacuum heat treatments. A previous study by Ngene et al. on the $LiBH_4$ mesoporous SiO_2 system demonstrated the ability to manipulate the density and properties of the surface functional groups of mesoporous SiO_2 via heat treatments at different temperatures. In their study, heat treatments were performed in an inert gas atmosphere and composites were synthesized by melt-infiltration.[36] In contrast, our study examined whether vacuum heat treatments and composite synthesis through ball milling could similarly influence ionic conductivity.

The surface properties of mesoporous Al_2O_3 were observed by ^1H MAS NMR. Figure 10 (a) shows ^1H MAS NMR spectra of pristine $LiBH_4$ and mesoporous Al_2O_3 treated following vacuum heat treatments at different temperatures. We prepared five different samples: untreated $LiBH_4$, 100 °C $LiBH_4$, untreated mesoporous Al_2O_3, 200 °C mesoporous Al_2O_3, and 700 °C mesoporous Al_2O_3. Each temperature represents the temperature of the vacuum heat treatment, with a holding time of 6 h for each condition. It should be noted that the melting points of $LiBH_4$ and mesoporous Al_2O_3 are 279 and 2,038 °C, respectively.

$LiBH_4$ remained relatively unchanged by heat treatment, while a significant change was observed for mesoporous Al_2O_3. Untreated mesoporous Al_2O_3 displayed a peak corresponding to physisorbed water at 4.6 ppm and two peaks representing hydroxy groups at 0.9 and 3.4 ppm. The 200 °C mesoporous Al_2O_3 only had one peak at 1.2 ppm, which corresponds to double-bridged hydroxy groups.[43,44] This indicates that the vacuum heat treatment at 200 °C removed physisorbed water. Figure 10 (a) shows that the ^1H MAS NMR intensities of the untreated mesoporous Al_2O_3, 200 °C mesoporous Al_2O_3, and 700 °C mesoporous Al_2O_3 are equal, suggesting that the triple-bridged hydroxy groups were lost after a 200 °C heat treatment but the double-bridged hydroxy groups remained. The 700 °C mesoporous Al_2O_3 showed no signal, with neither physisorbed water nor hydroxy groups observed. Figure 10 (b) shows the ionic conductivity of untreated $LiBH_4$ + untreated mesoporous Al_2O_3 (with high hydroxy group and physisorbed water density), 100 °C $LiBH_4$ + 200 °C mesoporous Al_2O_3 (with high hydroxy group density but low physisorbed water density), and 100 °C $LiBH_4$ + 700 °C mesoporous Al_2O_3 (with low hydroxy group density and physisorbed water density). The order of ionic conductivity was as follows: 100 °C $LiBH_4$ + 200 °C mesoporous Al_2O_3 > untreated $LiBH_4$ + untreated mesoporous Al_2O_3 > 100 °C $LiBH_4$ + 700 °C mesoporous Al_2O_3. This indicates that physisorbed water on Al_2O_3 negatively affected ionic conductivity, while surface hydroxy groups had a positive, albeit slight, influence.

3.5. Enhancement factor for the conductivity of $LiBH_4$-oxide composites

In our previous study, $LiBH_4$-ZrO_2 composites were synthesized by ball-milling and their ion conductivities were investigated.[28] However, specific surface area and pore volume were not measured at that time. As shown in Table S2, specific surface area, pore volume, and average pore diameter of ZrO_2 samples were measured from BET analysis. In addition, coating thickness of

$LiBH_4$ and pore filling rate of $LiBH_4$ in the case of $LiBH_4$-ZrO_2 composites were shown in Table S3. We compared the ionic conductivity of $LiBH_4$-Al_2O_3 composites with that of $LiBH_4$-ZrO_2 composites. Figure S7 (a) and (b) shows the ionic conductivity of those composites at 30 °C and 130 °C, respectively. Although milling conditions were slightly different from each other, the correlations with specific surface area and pore volume of oxide hosts were shown in both temperatures. The rough correlations with specific surface area and pore volume of the oxide suggests that size effects related to pore geometry would be main enhancement factors for improving the conductivity in this study. As shown in Figure S7 (a), it seemed that trend of $LiBH_4$-Al_2O_3 composites was slightly different from that of $LiBH_4$-ZrO_2 composites, thus the chemical effects arising from the $LiBH_4$-host oxide interactions may cause some differences. At 130 °C, the conductivities of Al_2O_3 composites were higher than those of ZrO_2 composites. This suggests nanoconfinement of $LiBH_4$ into the Al_2O_3 mesopores could be proceeded by heating the composites. In the previous study of ball-milled $LiBH_4$-metal oxide composites,[18] the clear correlations with specific surface area and pore volume were not observed. Although the correlation between conductivity and pore volume of the oxide was found in the $LiBH_4$-$LiNH_2$/SBA-15 composites synthesized by melt infiltration,[49] such kind of correlation was firstly found in the ball-milled $LiBH_4$-oxide composites as far as we know. Basically, the conductivity of $LiBH_4$-oxide composites prepared by melt infiltration was higher than that of ball-milled composites.[26] The recent study showed the difference of silica surface chemistry between $LiBH_4$-SiO_2 composites prepared via ball-milling and melt infiltration,[50] thus surface chemical bonding states with different processing methods also should be investigated in a future study.

4. Conclusions

The ionic conductivity of $LiBH_4$-Al_2O_3 composites was found to vary depending on the morphology of Al_2O_3. Among all composites, the 55 wt% mesoporous Al_2O_3 exhibited the highest ionic conductivity (4.6×10^{-5} S cm^{-1} at 30 °C) and lowest E_a for ionic conductivity (0.53 eV for 30–100 °C). XRD profiles showed that in all composites, the mixing of Al_2O_3 did not result in the formation of solid solutions or compounds, nor did it stabilize the HT phase at ambient temperatures. The XRD profile of 55 wt% mesoporous Al_2O_3 suggested the formation of a poorly crystalline (amorphous-like) interphase layer. From ^{7}Li static NMR, only the mesoporous composite showed motionally narrowed lines indicative of fast lithium ions. The fraction of these motionally narrowed lines, which represent highly mobile lithium ions, correlated with the specific surface area of the Al_2O_3 in each composite. Additionally, differences were observed in the chemical bonding state: the 55 wt% mesoporous composites showed a distinct low-field-shifted shoulder in ^{6}Li MAS NMR analysis. ^{1}H MAS NMR revealed the presence of physisorbed water and hydroxy groups on the surface of mesoporous Al_2O_3, though their effect on ionic conductivity was minimal. This suggests that the interaction of $LiBH_4$ with Al_2O_3, rather than the surface functional groups, plays a more significant role in improving ionic conductivity. From the

ionic conductivity plots classified according to specific surface area and pore volume of the host oxides (Al_2O_3 and ZrO_2), the correlations with specific surface area and pore volume of oxides were observed, thus size effects related to pore geometry would be mainly observed as the improved conductivity. To the best of our knowledge, such kind of correlations were firstly visualized for the ball-milled $LiBH_4$-oxide composites. Increasing the data points would clarify the detailed enhancement factors including the chemical effects arising from the $LiBH_4$-host oxide interactions.

The effects at the conductor-insulator interface can be explained by three hypotheses: the space charge regions, the formation of a ternary phase, and the stabilization of a HT phase as shown in the introduction part. Based on the XRD results, the stabilization of the high-temperature phase seems to be unlikely. The formation of amorphous-like interphase layer was suggested, and slightly different chemical bonding states were shown, thus the formation of a ternary phase could be a possible reason. This formation may be associated with the space charge regions, but further study is required.

Table 1. Average pore diameter, specific pore volume, and specific surface area of mesoporous Al_2O_3, gamma Al_2O_3, and nanofiber Al_2O_3 from BET analysis.

Sample	Average pore diameter (nm)	Specific pore volume ($cm^3\ g^{-1}$)	Specific surface area ($m^2\ g^{-1}$)
mesoporous Al_2O_3	5.9	0.47	324
gamma Al_2O_3	14.8	0.32	87
nanofiber Al_2O_3	7.6	0.12	61

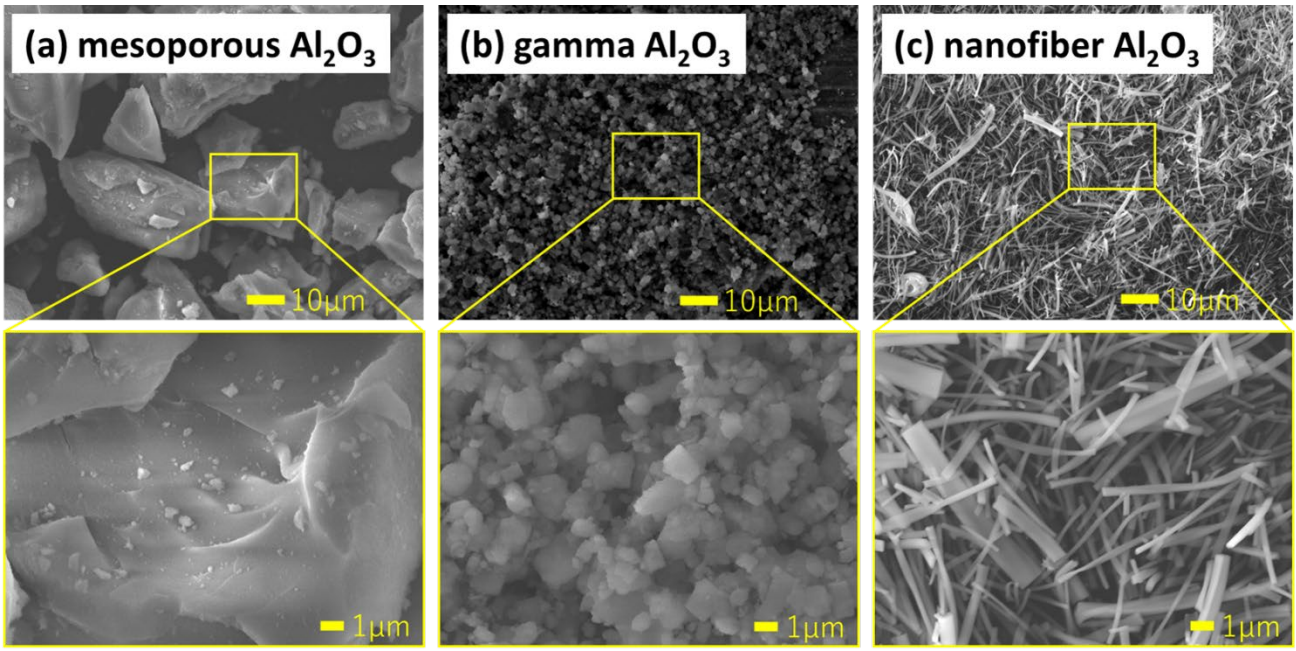

Figure 1. FE-SEM secondary electron images of the (a) mesoporous Al_2O_3, (b) gamma Al_2O_3, and (c) nanofiber Al_2O_3.

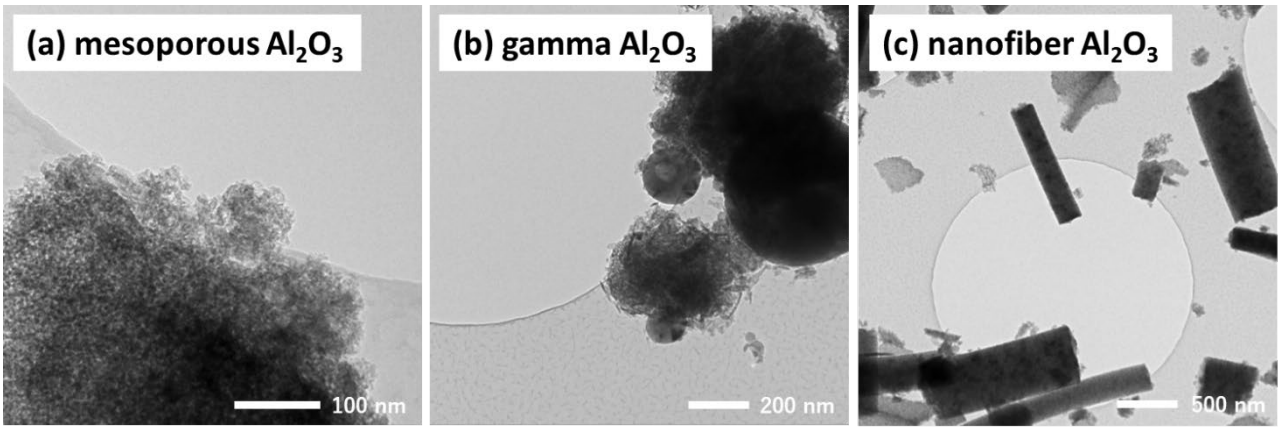

Figure 2. TEM images of the (a) mesoporous Al_2O_3, (b) gamma Al_2O_3, and (c) nanofiber Al_2O_3 samples.

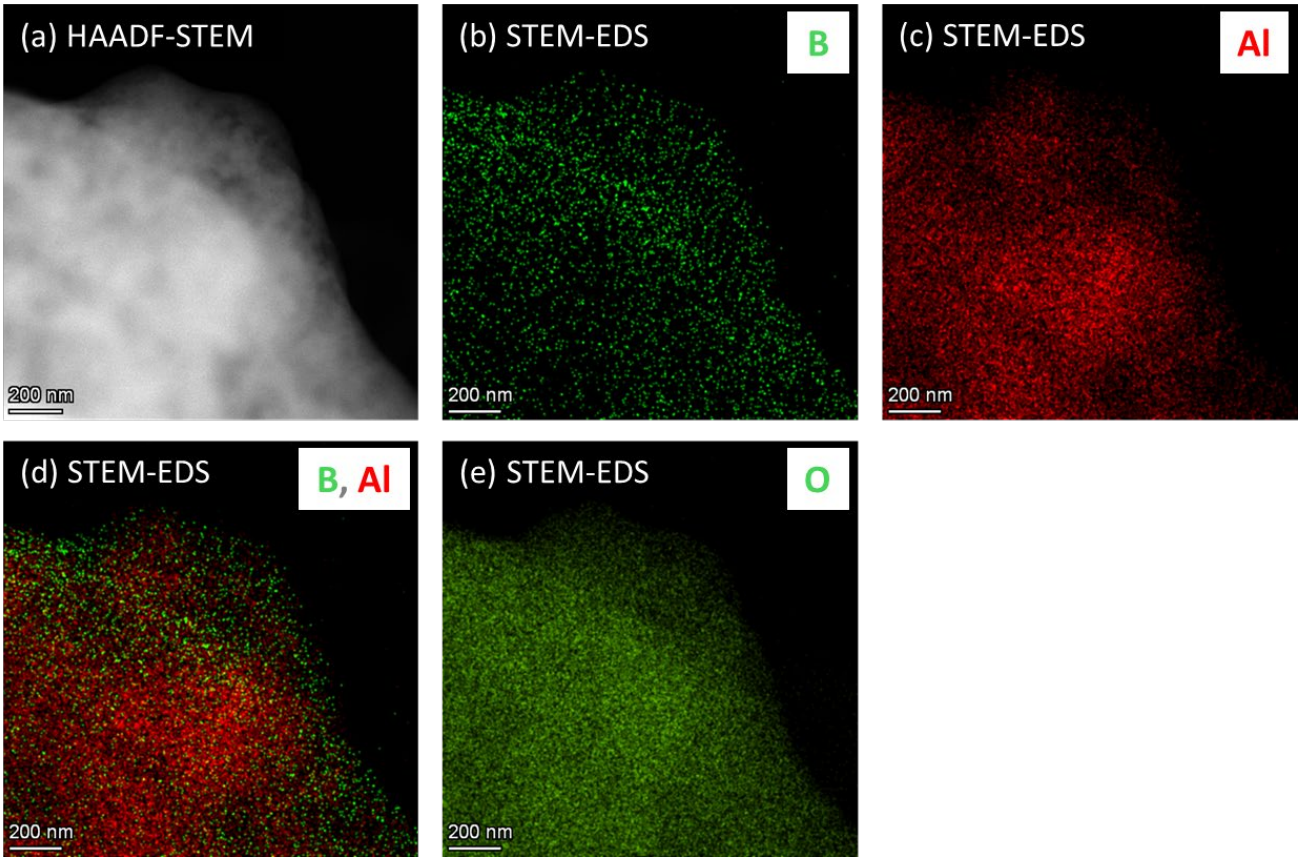

Figure 3. (a) HAADF-STEM image and STEM-EDS mapping images of (b) B, (c) Al, (d) overlap of B and Al, and (e) O of the $LiBH_4$-mesoporous Al_2O_3 composite.

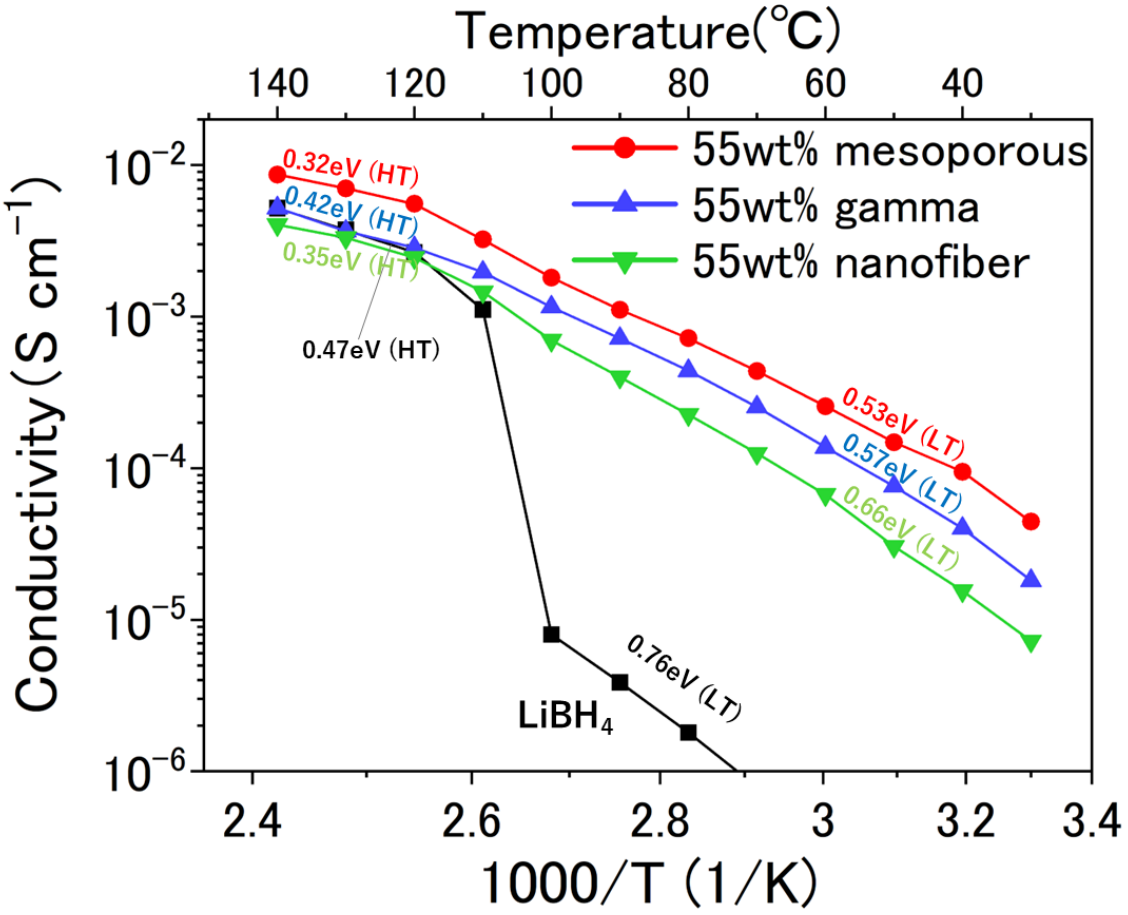

Figure 4. Arrhenius plots of ionic conductivity for pristine $LiBH_4$, 55 wt% mesoporous Al_2O_3, 55 wt% gamma Al_2O_3, and 55 wt% nanofiber Al_2O_3. The number in the figure indicates the E_a. Note that the E_a of all composites changed around the structural phase transition temperature of $LiBH_4$, thus the E_a of the LT phase and HT phase are derived in the range of 30–100 °C and 120–140 °C, respectively.

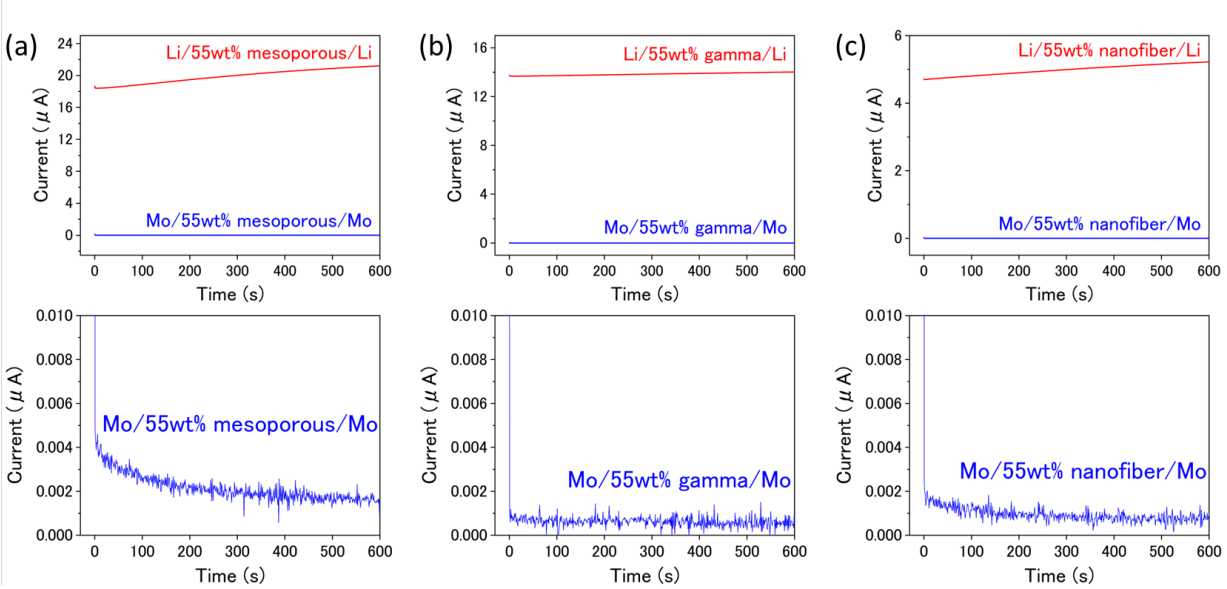

Figure 5. Time dependence of DC impedance of (a) 55 wt% mesoporous Al_2O_3, (b) 55 wt% gamma Al_2O_3, and (c) 55 wt% nanofiber Al_2O_3 after applying a constant voltage of +0.5 V for Li and Mo electrodes at 30 ℃. The figures below show the magnified profiles of each Mo electrode.

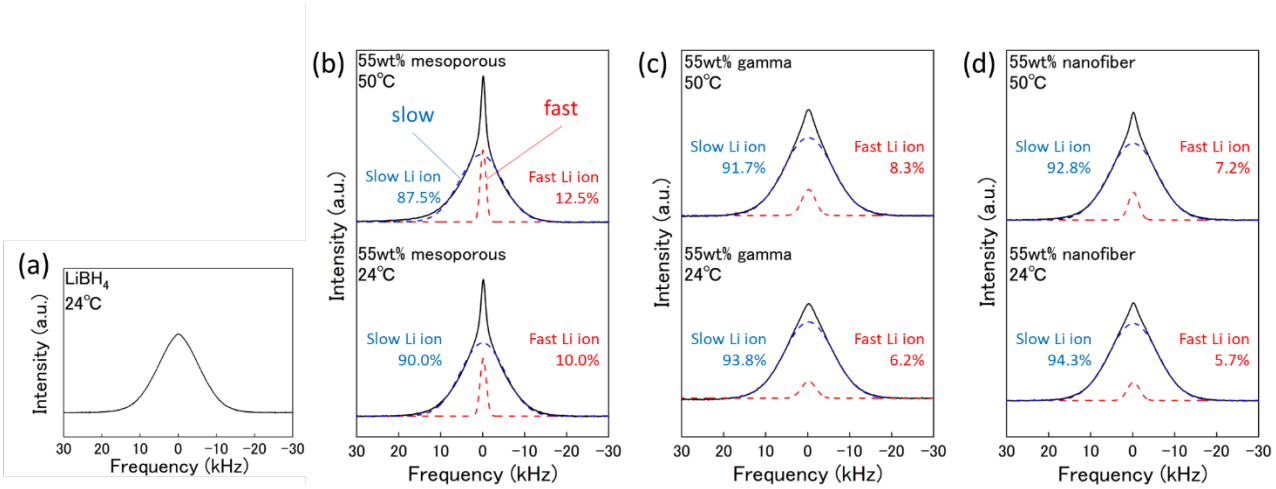

Figure 6. Temperature dependence of ^{7}Li static NMR spectra of (a) pristine $LiBH_4$, (b) 55 wt% mesoporous Al_2O_3, (c) 55 wt% gamma Al_2O_3, and (d) 55 wt% nanofiber Al_2O_3. The dashed lines show the deconvolution of the spectra using Gaussian functions.

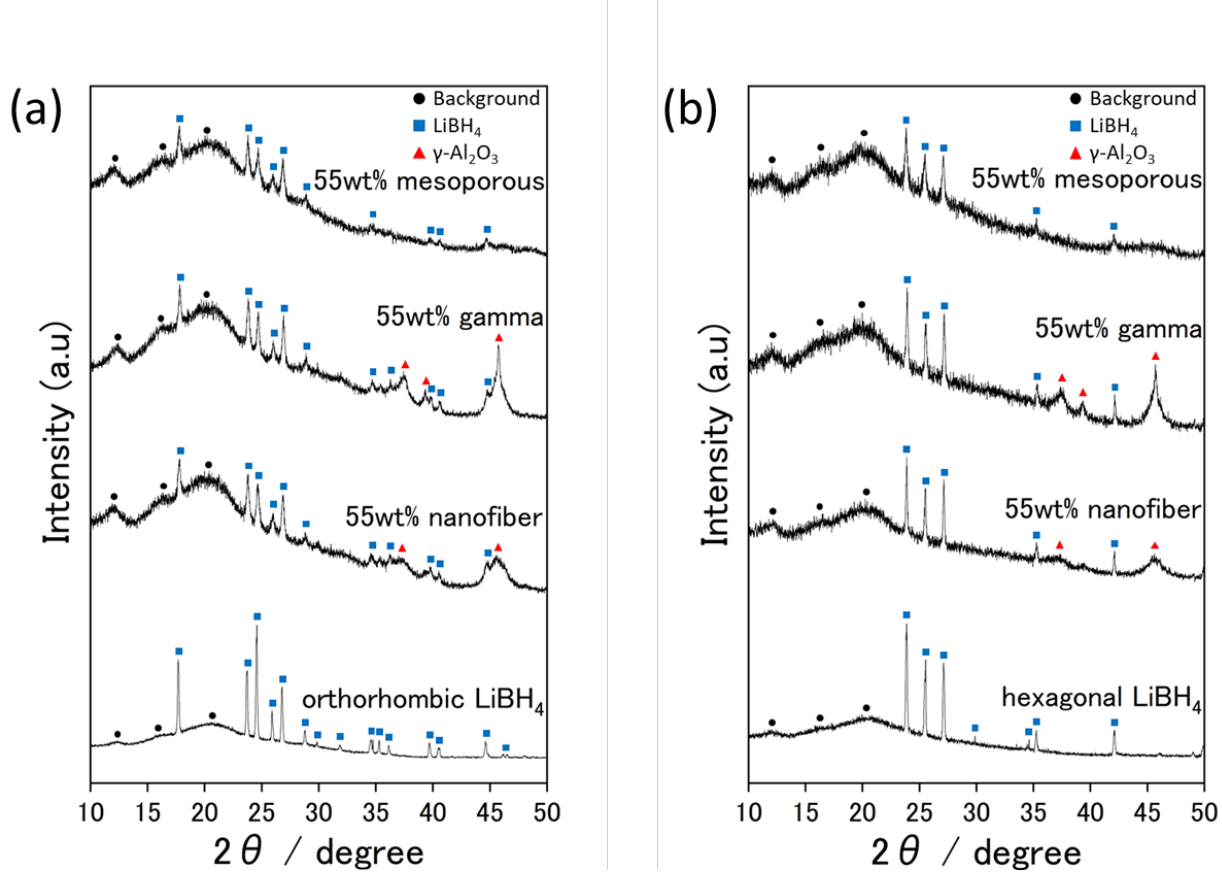

Figure 7. Temperature dependence XRD profiles: (a) orthorhombic $LiBH_4$, 55 wt% mesoporous Al_2O_3, 55 wt% gamma Al_2O_3, and 55 wt% nanofiber Al_2O_3 at room temperature and (b) hexagonal $LiBH_4$, 55 wt% mesoporous Al_2O_3, 55 wt% gamma Al_2O_3, and 55 wt% nanofiber Al_2O_3 at 140 °C.

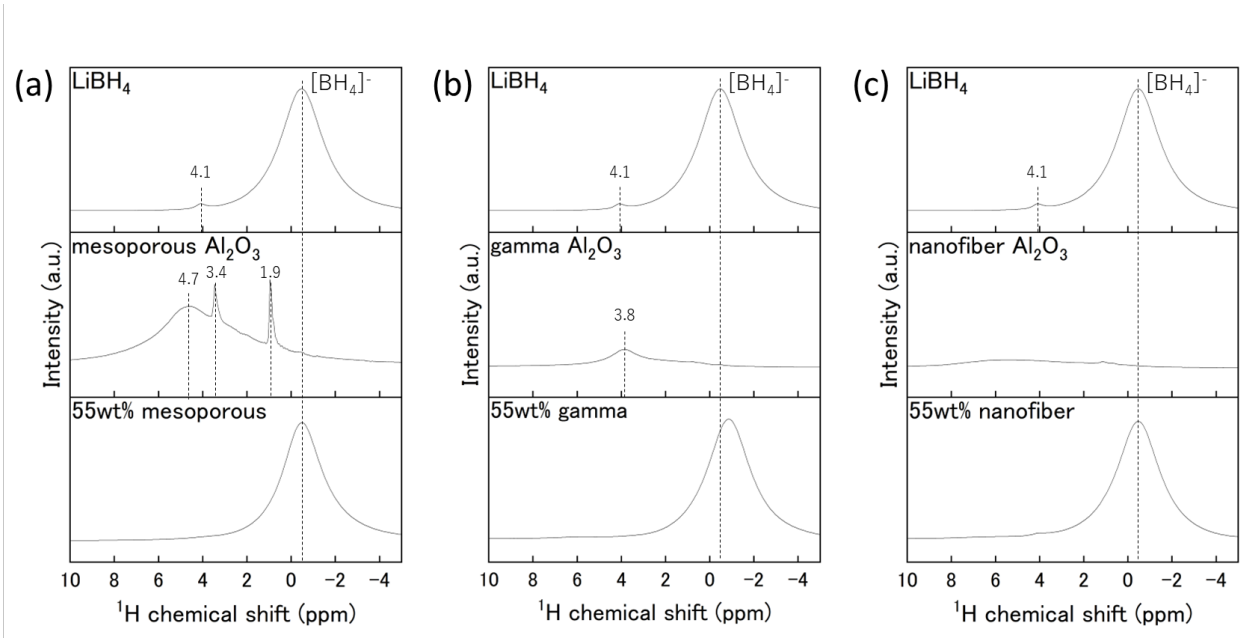

Figure 8. ^{1}H MAS NMR spectra of (a) pristine $LiBH_4$, mesoporous Al_2O_3, and 55 wt% mesoporous Al_2O_3; (b) pristine $LiBH_4$, gamma Al_2O_3, and 55 wt% gamma Al_2O_3; (c) pristine $LiBH_4$, nanofiber Al_2O_3, and 55 wt% nanofiber Al_2O_3 recorded at room temperature. The intensities are normalized for comparison.

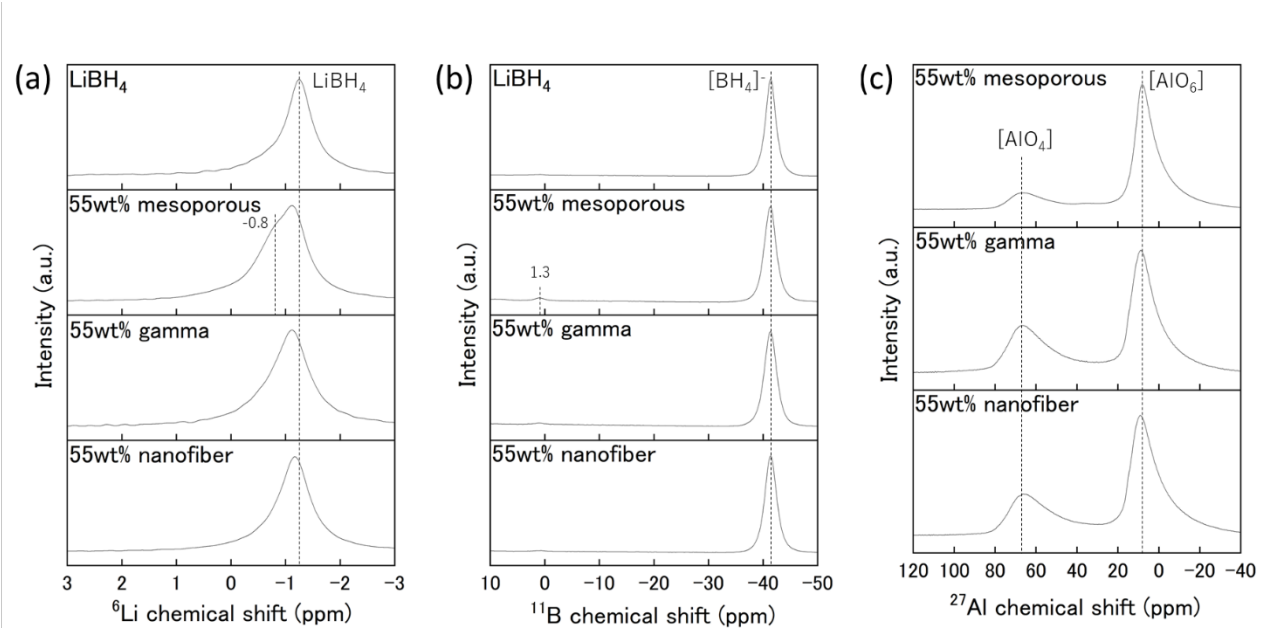

Figure 9. (a) ^{6}Li MAS, (b) ^{11}B MAS, and (c) ^{27}Al MAS NMR spectra of pristine $LiBH_4$, 55 wt% mesoporous Al_2O_3, 55 wt% gamma Al_2O_3, and 55 wt% nanofiber Al_2O_3 recorded at room temperature.

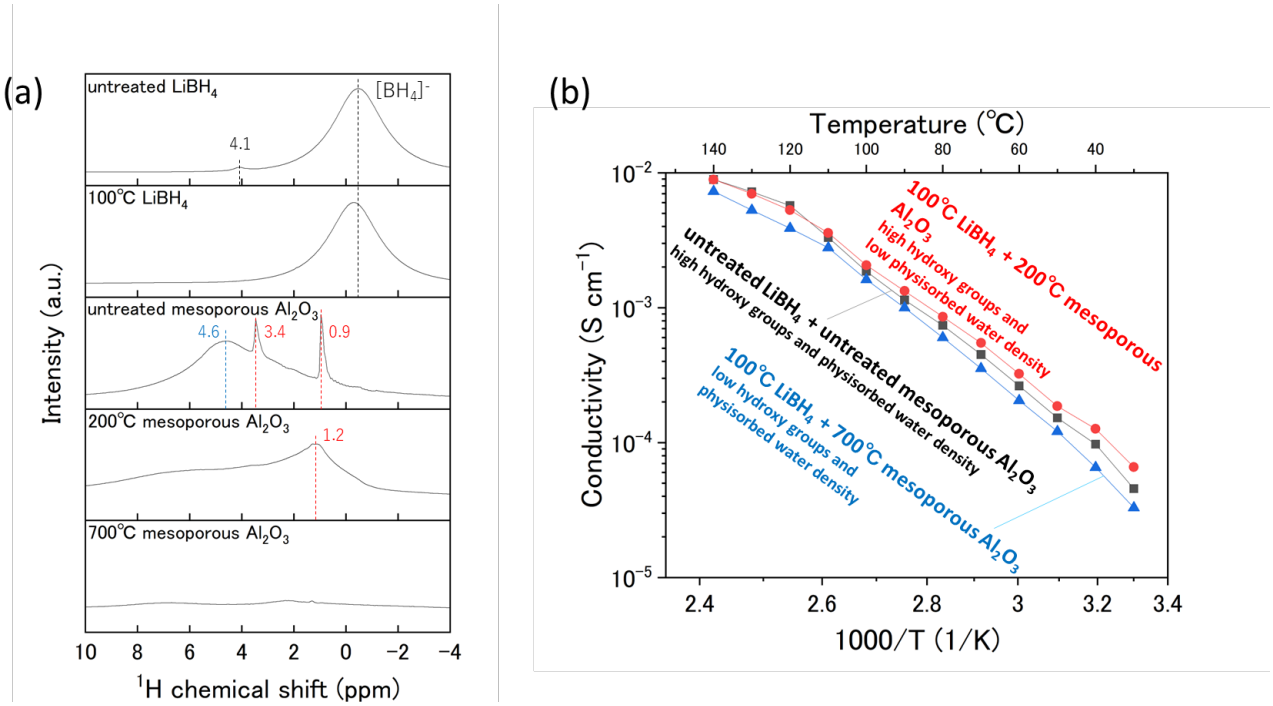

Figure 10. (a) ^{1}H MAS NMR spectra of untreated $LiBH_4$, 100 °C $LiBH_4$, untreated mesoporous Al_2O_3, 200 °C mesoporous Al_2O_3, and 700 °C mesoporous Al_2O_3 for 6 h. The spectra of untreated $LiBH_4$ and mesoporous Al_2O_3 are references from Figure 8. All intensity ranges on the vertical axes of the mesoporous Al_2O_3 are same. (b) Arrhenius plots of ionic conductivity for the untreated (untreated $LiBH_4$-untreated mesoporous Al_2O_3), 200 °C vacuum heated (100 °C $LiBH_4$-200 °C mesoporous Al_2O_3), and 700 °C vacuum heated (100 °C $LiBH_4$-700 °C mesoporous Al_2O_3) samples.

Supporting Information

TEM images of each Al_2O_3 composite, Arrhenius plots and ^7Li static NMR of 83 wt% Al_2O_3, and N_2 adsorption isotherms are presented in Supporting Information.

ORCID

Yuki Nakagawa: 0000-0001-5020-1458
Tamaki Shibayama: 0000-0003-3915-8924
Fangqin Guo: 0000-0001-8064-1470
Hiroki Miyaoka: 0000-0002-8480-7308
Takayuki Ichikawa: 0000-0003-3425-8758

Notes

The authors declare no competing financial interest.

Acknowledgments

This work was supported by JSPS KAKENHI Grant Number 24K08070. Part of this work was supported by the "Advanced Research Infrastructure for Materials and Nanotechnology in Japan (ARIM)" of the Ministry of the Ministry of Education, Culture, Sports, Science and Technology (MEXT), grant numbers JPMXP1223HK0022 and JPMXP1224HK0013 (Hokkaido University). The authors are thankful to Shuhei Shimoda for his help with BET experiments, Ryo Ota for his help with STEM experiments, Yurika Yamanouchi for her help with XRD experiments, and Naoya Nakagawa for his help with NMR experiments. We thank Edanz (https://jp.edanz.com/ac) for editing a draft of this manuscript.

Reference

(1) Inoue, T.; Mukai, K. Are All-Solid-State Lithium-Ion Batteries Really Safe?−verification by Differential Scanning Calorimetry with an All-Inclusive Microcell. *ACS Appl. Mater. Interfaces* **2017**, *9* (2), 1507–1515. https://doi.org/10.1021/acsami.6b13224.

(2) Chen, R.; Nolan, A. M.; Lu, J.; Wang, J.; Yu, X.; Mo, Y.; Chen, L.; Huang, X.; Li, H. The Thermal Stability of Lithium Solid Electrolytes with Metallic Lithium. *Joule* **2020**, *4* (4), 812–821. https://doi.org/10.1016/j.joule.2020.03.012.

(3) Tan, D. H. S.; Banerjee, A.; Chen, Z.; Meng, Y. S. From Nanoscale Interface Characterization to Sustainable Energy Storage Using All-Solid-State Batteries. *Nat. Nanotech*. **2020,** *15*, 170–180. https://doi.org/10.1038/s41565-020-0657-x.

(4) Kisu, K.; Kim, S.; Oguchi, H.; Toyama, N.; Orimo, S. ichi. Interfacial Stability between $LiBH_4$-Based Complex Hydride Solid Electrolytes and Li Metal Anode for All-Solid-State Li Batteries. *J. Power Sources* **2019**, *436*, 226821. https://doi.org/10.1016/j.jpowsour.2019.226821.

(5) Matsuo, M.; Nakamori, Y.; Orimo, S. I.; Maekawa, H.; Takamura, H. Lithium Superionic Conduction in Lithium Borohydride Accompanied by Structural Transition. *Appl. Phys. Lett.* **2007**, *91* (22), 224103. https://doi.org/10.1063/1.2817934.

(6) Verdal, N.; Her, J. H.; Stavila, V.; Soloninin, A. V.; Babanova, O. A.; Skripov, A. V.; Udovic, T. J.; Rush, J. J. Complex High-Temperature Phase Transitions in $Li_2B_{12}H_{12}$ and $Na_2B_{12}H_{12}$. *J. Solid State Chem.* **2014**, *212*, 81–91. https://doi.org/10.1016/j.jssc.2014.01.006.

(7) Kim, S.; Toyama, N.; Oguchi, H.; Sato, T.; Takagi, S.; Ikeshoji, T.; Orimo, S. I. Fast Lithium-Ion Conduction in Atom-Deficient Closo-Type Complex Hydride Solid Electrolytes. *Chem. Mater.* **2018**, *30* (2), 386–391. https://doi.org/10.1021/acs.chemmater.7b03986.

(8) Nakagawa, Y.; Kimura, T.; Isobe, S.; Shibayama, T. Effects of Defective Boron Nitride Additives on Lithium-Ion Conductivity and Hydrogen-Desorption Properties of $LiAlH_4$. *J. Phys. Chem. C* **2020**, *124* (19), 10398–10407. https://doi.org/10.1021/acs.jpcc.0c02312.

(9) Li, W.; Wu, G.; Xiong, Z.; Feng, Y. P.; Chen, P. Li + Ionic Conductivities and Diffusion Mechanisms in Li-Based Imides and Lithium Amide. *Phys. Chem. Chem. Phys.* **2012**, *14* (5), 1596–1606. https://doi.org/10.1039/c2cp23636b.

(10) Zhang, T.; Wang, Y.; Song, T.; Miyaoka, H.; Shinzato, K.; Miyaoka, H.; Ichikawa, T.; Shi, S.; Zhang, X.; Isobe, S.; Hashimoto, N.; Kojima, Y. Ammonia, a Switch for Controlling High Ionic Conductivity in Lithium Borohydride Ammoniates. *Joule* **2018**, *2* (8), 1522–1533. https://doi.org/10.1016/j.joule.2018.04.015.

(11) Nakagawa, Y.; Kimura, T.; Ohki, T.; Isobe, S.; Shibayama, T. Effect of Mechanical Milling on Lithium-Ion Conductivity of $LiAlH_4$. *Solid State Ion.* **2021**, *365*, 115656. https://doi.org/10.1016/j.ssi.2021.115656.

(12) Zou, S.; Yang, Y.; Wang, J.; Zhou, X.; Wan, X.; Zhu, M.; Liu, J. In Situ Polymerization of Solid-State Polymer Electrolytes for Lithium Metal Batteries: A Review. *Energy Environ. Sci*. **2024,** *17*, 4426–4460. https://doi.org/10.1039/d4ee00822g.

(13) Zhang, D.; Liu, Y.; Sun, Z.; Liu, Z.; Xu, X.; Xi, L.; Ji, S.; Zhu, M.; Liu, J. Eutectic-Based Polymer Electrolyte with the Enhanced Lithium Salt Dissociation for High-Performance Lithium Metal Batteries. *Angew. Chem. Int. Ed.* **2023**, *62* (44), e202310006. https://doi.org/10.1002/anie.202310006.

(14) Xi, L.; Li, Y.; Zhang, D.; Liu, Z.; Xu, X.; Liu, J. The Contact Interface Engineering of All-Sulfide-Based Solid State Batteries via Infiltrating Dissoluble Sulfide Electrolyte. *Energy Environ. Mater.* **2023**, *6* (6), e12461. https://doi.org/10.1002/eem2.12461.

(15) Gulino, V.; Wolczyk, A.; Golov, A. A.; Eremin, R. A.; Palumbo, M.; Nervi, C.; Blatov, V. A.; Proserpio, D. M.; Baricco, M. Combined DFT and Geometrical-Topological Analysis of Li-Ion Conductivity in Complex Hydrides. *Inorg. Chem. Front.* **2020**, *7* (17), 3115–3125. https://doi.org/10.1039/d0qi00577k.

(16) Tang, W. S.; Matsuo, M.; Wu, H.; Stavila, V.; Unemoto, A.; Orimo, S. I.; Udovic, T. J. Stabilizing Lithium and Sodium Fast-Ion Conduction in Solid Polyhedral-Borate Salts at Device-

Relevant Temperatures. *Energy Storage Mater.* **2016**, *4*, 79–83. https://doi.org/10.1016/j.ensm.2016.03.004.

(17) Lee, Y. S.; Cho, Y. W. Fast Lithium Ion Migration in Room Temperature $LiBH_4$. *J. Phys. Chem. C* **2017**, *121* (33), 17773–17779. https://doi.org/10.1021/acs.jpcc.7b06328.

(18) Gulino, V.; Barberis, L.; Ngene, P.; Baricco, M.; De Jongh, P. E. Enhancing Li-Ion Conductivity in $LiBH_4$-Based Solid Electrolytes by Adding Various Nanosized Oxides. *ACS Appl. Energy Mater.* **2020**, *3* (5), 4941–4948. https://doi.org/10.1021/acsaem.9b02268.

(19) Gulino, V.; Brighi, M.; Dematteis, E. M.; Murgia, F.; Nervi, C.; Černý, R.; Baricco, M. Phase Stability and Fast Ion Conductivity in the Hexagonal $LiBH_4$-LiBr-LiCl Solid Solution. *Chem. Mater.* **2019**, *31* (14), 5133–5144. https://doi.org/10.1021/acs.chemmater.9b01035.

(20) Rude, L. H.; Groppo, E.; Arnbjerg, L. M.; Ravnsbæk, D. B.; Malmkjær, R. A.; Filinchuk, Y.; Baricco, M.; Besenbacher, F.; Jensen, T. R. Iodide Substitution in Lithium Borohydride, $LiBH_4$-LiI. *J. Alloys Compd.* **2011**, *509* (33), 8299–8305. https://doi.org/10.1016/j.jallcom.2011.05.031.

(21) Maekawa, H.; Matsuo, M.; Takamura, H.; Ando, M.; Noda, Y.; Karahashi, T.; Orimo, S. I. Halide-Stabilized $LiBH_4$, a Room-Temperature Lithium Fast-Ion Conductor. *J. Am. Chem. Soc.* **2009**, *131* (3), 894–895. https://doi.org/10.1021/ja807392k.

(22) Matsuo, M.; Takamura, H.; Maekawa, H.; Li, H. W.; Orimo, S. I. Stabilization of Lithium Superionic Conduction Phase and Enhancement of Conductivity of $LiBH_4$ by LiCl Addition. *Appl. Phys. Lett.* **2009**, *94* (8), 084103. https://doi.org/10.1063/1.3088857.

(23) Sveinbjörnsson, D.; Myrdal, J. S. G.; Blanchard, D.; Bentzen, J. J.; Hirata, T.; Mogensen, M. B.; Norby, P.; Orimo, S. I.; Vegge, T. Effect of Heat Treatment on the Lithium Ion Conduction of the $LiBH_4$-LiI Solid Solution. *J. Phys. Chem. C* **2013**, *117* (7), 3249–3257. https://doi.org/10.1021/jp310050g.

(24) Epp, V.; Wilkening, M. Motion of Li^+ in Nanoengineered $LiBH_4$ and $LiBH_4$:Al_2O_3 Comparison with the Microcrystalline Form. *ChemPhysChem* **2013**, *14* (16), 3706–3713. https://doi.org/10.1002/cphc.201300743.

(25) Blanchard, D.; Nale, A.; Sveinbjörnsson, D.; Eggenhuisen, T. M.; Verkuijlen, M. H. W.; Suwarno; Vegge, T.; Kentgens, A. P. M.; De Jongh, P. E. Nanoconfined $LiBH_4$ as a Fast Lithium Ion Conductor. *Adv. Funct. Mater.* **2015**, *25* (2), 184–192. https://doi.org/10.1002/adfm.201402538.

(26) Choi, Y. S.; Lee, Y. S.; Oh, K. H.; Cho, Y. W. Interface-Enhanced Li Ion Conduction in a $LiBH_4$-SiO_2 Solid Electrolyte. *Phys. Chem. Chem. Phys.* **2016**, *18* (32), 22540–22547. https://doi.org/10.1039/c6cp03563a.

(27) Dansirima, P.; Kristensen, L. G.; Grinderslev, J. B.; Skibsted, J.; Utke, R.; Jensen, T. R. Nanoconfinement of an Ammine Magnesium Borohydride Composite Electrolyte in a Mesoporous Silica Scaffold. *Commun. Mater.* **2024**, *5* (1), 160. https://doi.org/10.1038/s43246-024-00601-5.

(28) Nakagawa, Y.; Sendo, T.; Shibayama, T. Enhanced Li-Ion Conductivity in $LiBH_4$-ZrO_2 Nanocomposites and Nanoscale Li Imaging by Energy-Filtered Transmission Electron Microscopy. *Chem. Commun.* **2023**, *59* (73), 10912–10915. https://doi.org/10.1039/d3cc02860g.

(29) Choi, Y. S.; Lee, Y. S.; Choi, D. J.; Chae, K. H.; Oh, K. H.; Cho, Y. W. Enhanced Li Ion Conductivity in $LiBH_4$-Al_2O_3 Mixture via Interface Engineering. *J. Phys. Chem. C* **2017**, *121* (47), 26209–26215. https://doi.org/10.1021/acs.jpcc.7b08862.

(30) Zettl, R.; Gombotz, M.; Clarkson, D.; Greenbaum, S. G.; Ngene, P.; De Jongh, P. E.; Wilkening, H. M. R. Li-Ion Diffusion in Nanoconfined $LiBH_4$-LiI/Al_2O_3: From 2D Bulk Transport to 3D Long-Range Interfacial Dynamics. *ACS Appl. Mater. Interfaces* **2020**, *12* (34), 38570–38583. https://doi.org/10.1021/acsami.0c10361.

(31) Zettl, R.; De Kort, L.; Gombotz, M.; Wilkening, H. M. R.; De Jongh, P. E.; Ngene, P. Combined Effects of Anion Substitution and Nanoconfinement on the Ionic Conductivity of Li-Based Complex Hydrides. *J. Phys. Chem. C* **2020**, *124* (5), 2806–2816. https://doi.org/10.1021/acs.jpcc.9b10607.

(32) De Kort, L. M.; Gulino, V.; de Jongh, P. E.; Ngene, P. Ionic Conductivity in Complex Metal Hydride-Based Nanocomposite Materials: The Impact of Nanostructuring and Nanocomposite Formation. *J. Alloys Compd.* **2022**, *901*, 163474. https://doi.org/10.1016/j.jallcom.2021.163474.

(33) Zou, Z.; Li, Y.; Lu, Z.; Wang, D.; Cui, Y.; Guo, B.; Li, Y.; Liang, X.; Feng, J.; Li, H.; Nan, C. W.; Armand, M.; Chen, L.; Xu, K.; Shi, S. Mobile Ions in Composite Solids. *Chem. Rev*. **2020,** *120* (9), 4169–4221. https://doi.org/10.1021/acs.chemrev.9b00760.

(34) De Kort, L. M.; Lazemi, M.; Longo, A.; Gulino, V.; Rodenburg, H. P.; Blanchard, D.; Sahle, C.; Sundermann, M.; Gretarsson, H.; van der Eerden, A. M. J.; Elnaggar, H.; de Groot, F. M. F.; Ngene, P. Deciphering the Origin of Interface-Induced High Li and Na Ion Conductivity in Nanocomposite Solid Electrolytes Using X-Ray Raman Spectroscopy. *Adv. Energy Mater.* **2024**, *14* (9), 2303381. https://doi.org/10.1002/aenm.202303381.

(35) Lambregts, S. F. H.; Van Eck, E. R. H.; Suwarno; Ngene, P.; De Jongh, P. E.; Kentgens, A. P. M. Phase Behavior and Ion Dynamics of Nanoconfined $LiBH_4$ in Silica. *J. Phys. Chem. C* **2019**, *123* (42), 25559–25569. https://doi.org/10.1021/acs.jpcc.9b06477.

(36) Ngene, P.; Lambregts, S. F. H.; Blanchard, D.; Vegge, T.; Sharma, M.; Hagemann, H.; De Jongh, P. E. The Influence of Silica Surface Groups on the Li-Ion Conductivity of $LiBH_4$/SiO_2 Nanocomposites. *Phys. Chem. Chem. Phys.* **2019**, *21* (40), 22456–22466. https://doi.org/10.1039/c9cp04235k.

(37) Breuer, S.; Pregartner, V.; Lunghammer, S.; Wilkening, H. M. R. Dispersed Solid Conductors: Fast Interfacial Li-Ion Dynamics in Nanostructured LiF and LiF γ-Al_2O_3 Composites. *J. Phys. Chem. C* **2019**, *123* (9), 5222–5230. https://doi.org/10.1021/acs.jpcc.8b10978.

(38) Zettl, R.; Hogrefe, K.; Gadermaier, B.; Hanzu, I.; Ngene, P.; De Jongh, P. E.; Wilkening, H. M. R.

Conductor-Insulator Interfaces in Solid Electrolytes: A Design Strategy to Enhance Li-Ion Dynamics in Nanoconfined $LiBH_4/Al_2O_3$. *J. Phys. Chem. C* **2021**, *125* (27), 15052–15060. https://doi.org/10.1021/acs.jpcc.1c03789.

(39) Lambregts, S. F. H.; Van Eck, E. R. H.; Ngene, P.; Kentgens, A. P. M. The Nature of Interface Interactions Leading to High Ionic Conductivity in $LiBH_4/SiO_2$ Nanocomposites. *ACS Appl. Energy Mater.* **2022**, *5* (7), 8057–8066. https://doi.org/10.1021/acsaem.2c00527.

(40) Liu, M.; Yang, H. Facile Synthesis and Characterization of Macro-Mesoporous γ-Al_2O_3. *Colloids Surf. A Physicochem. Eng. Asp.* **2010**, *371* (1–3), 126–130. https://doi.org/10.1016/j.colsurfa.2010.09.022.

(41) Solovyov, L. A.; Belousov, O. V.; Dinnebier, R. E.; Shmakov, A. N.; Kirik, S. D. X-Ray Diffraction Structure Analysis of MCM-48 Mesoporous Silica. *J. Phys. Chem. B* **2005**, *109* (8), 3233–3237. https://doi.org/10.1021/jp0482868.

(42) Liu, X.; Majzoub, E. H.; Stavila, V.; Bhakta, R. K.; Allendorf, M. D.; Shane, D. T.; Conradi, M. S.; Verdal, N.; Udovic, T. J.; Hwang, S. J. Probing the Unusual Anion Mobility of $LiBH_4$ Confined in Highly Ordered Nanoporous Carbon Frameworks via Solid State NMR and Quasielastic Neutron Scattering. *J. Mater. Chem. A* **2013**, *1* (34), 9935–9941. https://doi.org/10.1039/c3ta12051a.

(43) Trébosc, J.; Wiench, J. W.; Huh, S.; Lin, V. S. Y.; Pruski, M. Solid-State MMR Study of MCM-41-Type Mesoporous Silica Nanoparticles. *J. Am. Chem. Soc.* **2005**, *127* (9), 3057–3068. https://doi.org/10.1021/ja043567e.

(44) Zhao, Z.; Xiao, D.; Chen, K.; Wang, R.; Liang, L.; Liu, Z.; Hung, I.; Gan, Z.; Hou, G. Nature of Five-Coordinated Al in γ-Al_2O_3 Revealed by Ultra-High-Field Solid-State NMR. *ACS Cent. Sci.* **2022**, *8* (6), 796–803. https://doi.org/10.1021/acscentsci.1c01497.

(45) Seong, W. M.; Kim, Y.; Manthiram, A. Impact of Residual Lithium on the Adoption of High-Nickel Layered Oxide Cathodes for Lithium-Ion Batteries. *Chem. Mater.* **2020,** *32* (22), 9479–9489. https://doi.org/10.1021/acs.chemmater.0c02808.

(46) Choi, Y. J.; Lu, J.; Sohn, H. Y.; Fang, Z. Z.; Kim, C.; Bowman, R. C.; Hwang, S. J. Reaction Mechanisms in the $Li_3AlH_6/LiBH_4$ and $Al/LiBH_4$ Systems for Reversible Hydrogen Storage. Part 2: Solid-State NMR Studies. *J. Phys. Chem. C* **2011**, *115* (13), 6048–6056. https://doi.org/10.1021/jp109113f.

(47) Lai, Q.; Alligier, D.; Aguey-Zinsou, K. F.; Demirci, U. B. Hydrogen Generation from a Sodium Borohydride-Nickel Core@shell Structure under Hydrolytic Conditions. *Nanoscale Adv.* **2019**, *1* (7), 2707–2717. https://doi.org/10.1039/c9na00037b.

(48) Hiraishi, N.; Sayed, M.; Hill, R.; Tagami, J.; Hayashi, F. Interactions of Boron Released from Surface Pre-Reacted Glass Ionomer with Enamel/Dentin and Its Effect on PH. *Sci. Rep.* **2021**, *11* (1), 15734. https://doi.org/10.1038/s41598-021-95279-x.

(49) De Kort, L. M.; Harmel, J.; De Jongh, P. E.; Ngene, P. The Effect of Nanoscaffold Porosity and Surface Chemistry on the Li-Ion Conductivity of $LiBH_4$-$LiNH_2$/Metal Oxide

Nanocomposites. *J. Mater. Chem. A* **2020**, *8* (39), 20687–20697. https://doi.org/10.1039/d0ta07600g.

(50) Lambregts, S. F. H.; de Kort, L. M.; Winkelmann, F.; Felderhoff, M.; Ngene, P.; van Eck, E. R. H.; Kentgens, A. P. M. Effect of Preparation Methods on the Interface of $LiBH_4/SiO_2$ Nanocomposite Solid Electrolytes. *J. Phys. Chem. C* **2024**, *128* (29), 12186–12193. https://doi.org/10.1021/acs.jpcc.4c02667.

Table of Contents

Effects of oxide morphology on lithium-ion conductivity of $LiBH_4$-Al_2O_3 composites

Hiroki Mizuochi, Yuki Nakagawa, Tamaki Shibayama, Yuchen Yao, Fangqin Guo, Hiroki Miyaoka, Takayuki Ichikawa